RESEARCH ARTICLE

Key Points:
- A methodology for regional GPP estimation and uncertainty analysis was evaluated
- The 6-year GPP in Tibetan grasslands are estimated using modified VPM model
- The uncertainty of modeled GPP is quantified and traced to specific model input

Correspondence to:
G. Yu,
yugr@igsnrr.ac.cn

Large-scale estimation and uncertainty analysis of gross primary production in Tibetan alpine grasslands

Honglin He[1], Min Liu[2], Xiangming Xiao[3], Xiaoli Ren[1,4], Li Zhang[1], Xiaomin Sun[1], Yuanhe Yang[5], Yingnian Li[6], Liang Zhao[6], Peili Shi[1], Mingyuan Du[7], Yaoming Ma[8], Mingguo Ma[9], Yu Zhang[9], and Guirui Yu[1]

[1]Key Laboratory of Ecosystem Network Observation and Modeling, Institute of Geographic Sciences and Natural Resources Research, Chinese Academy of Sciences, Beijing, China, [2]Shanghai Key Laboratory for Urban Ecological Processes and Eco-Restoration, East China Normal University, Shanghai, China, [3]Department of Botany and Microbiology, University of Oklahoma, Norman, Oklahoma, USA, [4]College of Resources and Environment, University of Chinese Academy of Sciences, Beijing, China, [5]State Key Laboratory of Vegetation and Environmental Change, Institute of Botany, Chinese Academy of Sciences, Beijing, China, [6]Northwest Plateau Institute of Biology, Chinese Academy of Sciences, Xining, Qinghai, China, [7]National Institute for Agro-Environmental Science, Ibaraki, Tsukuba, Japan, [8]Key Laboratory of Tibetan Environment Changes and Land Surface Processes, Institute of Tibetan Plateau Research, Chinese Academy of Sciences, Beijing, China, [9]Cold and Arid Regions Environmental and Engineering Research Institute, Chinese Academy of Sciences, Lanzhou, Gansu, China

Abstract Gross primary production (GPP) is an important parameter for carbon cycle and climate change research. Previous estimations of GPP on the Tibetan Plateau were usually reported without quantitative uncertainty analyses. This study sought to quantify the uncertainty and its partitioning in GPP estimation across Tibetan alpine grasslands during 2003–2008 with the modified Vegetation Photosynthesis Model (VPM). Monte Carlo analysis was used to provide a quantitative assessment of the uncertainty in model simulations, and Sobol' variance decomposition method was applied to determine the relative contribution of each source of uncertainty to the total uncertainty. The results showed that the modified VPM successfully reproduced the seasonal dynamics and magnitude of GPP of 10 flux tower sites on the plateau ($R^2 = 0.77 - 0.95$, $p < 0.001$). The 6 year mean GPP in Tibetan alpine grasslands was estimated at 223.3 Tg C yr^{-1} (312.3 g C m^{-2} yr^{-1}). The mean annual GPP increased from western to eastern plateau, with the increase of annual temperature and precipitation and the decrease of elevation, while the decrease of GPP from southern to northern plateau was primarily driven by air temperature. Furthermore, the mean relative uncertainty of the annual GPP was 18.30%, with larger uncertainty occurring in regions with lower GPP. Photosynthetic active radiation, enhanced vegetation index, and the maximum light use efficiency (LUE) are the primary sources of uncertainty in GPP estimation, contributing 36.84%, 26.86%, and 21.99%, respectively. This emphasizes the importance of uncertainty in driving variables as well as that of maximum LUE in LUE model simulation.

1. Introduction

Accurate evaluation of carbon dynamics over regions is of major concern in current global climate change research [*Denman et al.*, 2007]. Gross primary production (GPP), defined as the overall rate of carbon fixation through the process of vegetation photosynthesis, is the largest carbon flux driving several ecosystem functions [*Beer et al.*, 2010]. Continuous monitoring and accurate estimation of GPP is needed to improve our understanding of the feedbacks between the terrestrial ecosystem and the atmosphere in the context of global climate change, informing both policy and management decisions [*Canadell et al.*, 2000; *Denman et al.*, 2007]. Eddy covariance (EC) technique is a key atmospheric measurement technique to assess net ecosystem CO_2 exchange (NEE), and NEE data can be partitioned into GPP and ecosystem respiration [*Falge et al.*, 2002a; *Falge et al.*, 2002b]. However, flux tower sites only provide integrated CO_2 flux measurements over footprints (the upwind area measured by a flux tower) with sizes and shapes (ranging from hundreds of meters to several kilometers) that vary with the tower height, canopy physical characteristics, and wind velocity [*Davis et al.*, 2003; *Osmond et al.*, 2004]. To quantify the terrestrial carbon dynamics over large areas, we need to upscale flux observations from sites to regions [*Desai et al.*, 2008; *Xiao et al.*, 2008]. Generally, modeling is the
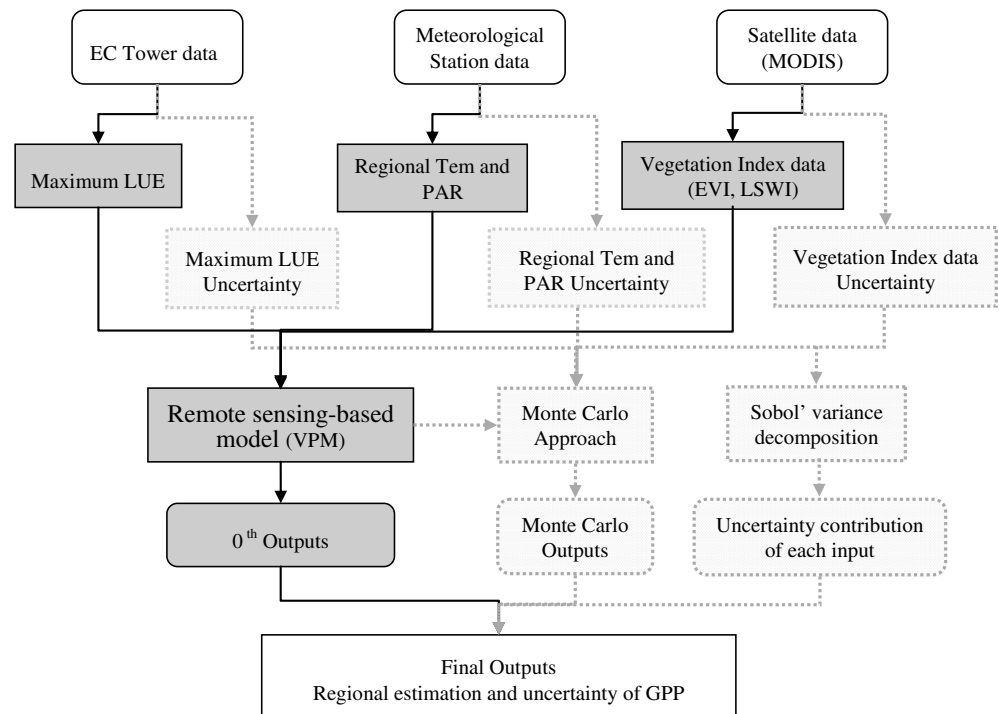
Figure 1. Flow diagram of the methodology used for GPP estimation and uncertainty analysis in Tibetan alpine grasslands.

commonly used approach for inferring GPP at larger spatial scales [*Beer et al.*, 2010; *Jung et al.*, 2008; *Wang et al.*, 2010; *Wylie et al.*, 2007; *Yang et al.*, 2007; *Zhang et al.*, 2011; *Zhuang et al.*, 2010].

Models applied for GPP estimation range in complexity from empirical models [*Wylie et al.*, 2007; *Yang et al.*, 2007], light use efficiency (LUE) models [*Xiao et al.*, 2004a; *Yuan et al.*, 2007] to process-based models [*Aber et al.*, 1996; *Cao and Woodward*, 1998; *Zhuang et al.*, 2003], with each type of models having advantages and deficiencies. LUE models in particular have been developed for monitoring regional GPP with relatively simple model structure and generally based on remote sensing products of high temporal-spatial resolution [*Mccallum et al.*, 2013; *Wang et al.*, 2010]. Trials in this direction have been made in Europe, North America, and the globe with aims to integrate flux tower data and remote sensing data for regional carbon budget research [*Beer et al.*, 2007; *Jung et al.*, 2008; *Papale and Valentini*, 2003; *Wang et al.*, 2010; *Yang et al.*, 2010].

However, due to the large spatial heterogeneity and temporal dynamics of ecosystems across complex regions, the simulations of terrestrial carbon budget at regional scale inevitably suffer from deficiencies and uncertainties [*Beven*, 2006; *Beven and Freer*, 2001]. Model predictions are associated with uncertainties resulting from model structure, input data, parameters, evaluation data, etc. [*Beven*, 1989; *Haan*, 1989; *Luis and McLaughlin*, 1992; *Shirmohammadi et al.*, 2006]. We are still far from providing an accurate estimation of regional GPP, which is still the focus of global carbon cycle research [*Beer et al.*, 2010; *Lin et al.*, 2011; *Reich*, 2010]. While numerous modeling studies have included uncertainty considerations [*Beer et al.*, 2010; *Groenendijk et al.*, 2011; *Mccallum et al.*, 2013], uncertainties are rarely quantified, especially at regional scale, and so it is difficult to determine how much confidence can be placed in the results [*Ogle et al.*, 2010]. The advancement of uncertainty analysis techniques in recent years provides promising tools for uncertainty quantification and partitioning in carbon flux estimation at regional scale [*Liburne and Tarantola*, 2009; *Saltelli*, 2002].

The purpose of this paper is twofold: (1) to provide a relatively accurate estimation for GPP in Tibetan alpine grasslands with a modified LUE model, based on eddy flux data, remote sensing, and meteorological data, and (2) to quantify the spatial uncertainty of regional GPP estimation and the relative contributions of each uncertainty source, addressing uncertainty in model parameters (maximum LUE) and input data (meteorological and remote sensing data). The flow diagram of the methodology used to estimate GPP and its uncertainty in Tibetan alpine grasslands was illustrated in Figure 1. First, spatiotemporal GPP variations over the study area were simulated with a modified LUE model—Vegetation Photosynthesis Model (VPM) [*Xiao et al.*,
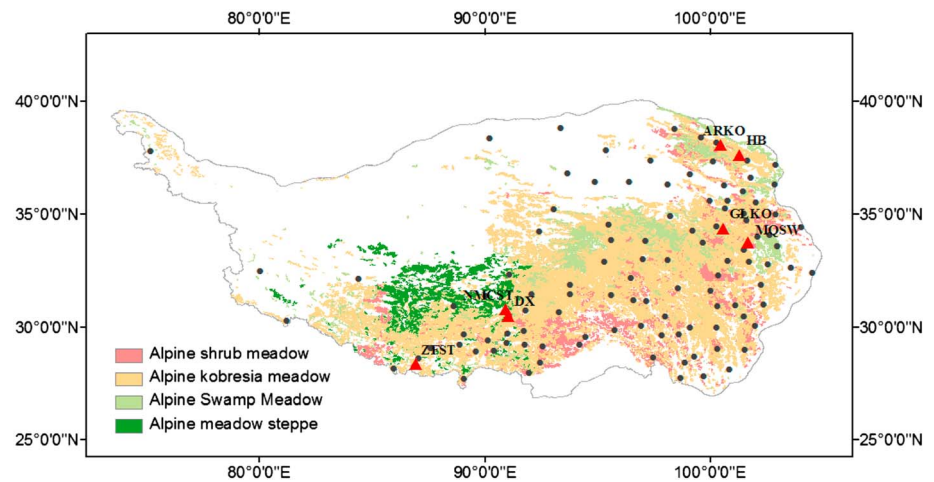
Figure 2. Spatial distributions of alpine grasslands on the Tibetan Plateau. Ten flux sites (filled red triangle symbol), three of them are located in HB (HBKO, HBSH, HBSW) and two of them are located in DX (DXSW, DXST), and 108 meteorological stations (filled black circle symbol) were plotted.

2004a, 2004b]. Second, coupled with the spatial uncertainty in model parameters derived from eddy covariance technique, meteorological observations, and MODIS products of vegetation and water indices, multiple results are simulated based on repeated random samplings from the probability distribution functions of model parameters and input data with Monte Carlo approach. Finally, the overall spatial uncertainty was partitioned into each uncertainty source with a variance decomposition method. Our analysis provides an alternative and quantitative fashion that can be used in uncertainty analysis of regional carbon dynamics evaluation.

2. Materials and Methods

2.1. Data Sets

2.1.1. Eddy Covariance Flux Measurements

In this study, we utilized 27 site-year data of 10 field sites collected in 2003–2010 on the Tibetan Plateau (Figure 2), with elevation ranging from 3000 to 4800 m, to estimate a model parameter (i.e., maximum LUE) and evaluate model performance. These flux sites represented the dominant alpine grasslands in the region:

Table 1. Main Characteristics of the 10 Flux Tower Sites Over the Tibetan Alpine Grasslands

Alpine Grassland Subtype	Site	Location	Elevation (m)	Canopy Height (m)	EC Height (m)	Study Period
Alpine kobresia meadow	HBKO	37.61°N 101.31°E	3148	0.2–0.3	2.2	2003–2005
	GLKO	34.35°N 100.56°E	3980	0.2–0.3	2.2	2007
	ARKO	38.04°N 100.46°E	3033	0.2–0.3	3.15	2008–2010
Alpine shrub meadow	HBSH	37.67°N 101.33°E	3293	0.6–0.7	2.2	2003–2007
Alpine swamp meadow	HBSW	37.61°N 101.33°E	3160	0.2–0.5	2.2	2004–2008
	DXSW	30.47°N 91.06°E	4286	0.2–0.5	2.1	2009–2010
	MQSW	33.76°N 101.68°E	3503	0.3–0.5	3.2	2010
Alpine meadow steppe	DXST	30.50°N 91.06°E	4333	<0.2	2.2	2004–2008
	ZFST	28.36°N 86.95°E	4293	<0.2	3.1	2009
	NMCST	30.77°N 90.96°E	4730	<0.2	3.1	2009

alpine kobresia meadow (HBKO, GLKO, and ARKO), alpine shrub meadow (HBSH), alpine swamp meadow (HBSW, DXSW, and MQSW), and alpine meadow steppe (DXST, ZFST, and NMCST). An overview of the characteristics of these 10 sites is given in Table 1.

Eddy covariance measurements of the surface-atmosphere exchanges of CO_2, H_2O, and energy have been collected at these tower sites. The measurement system is described in detail by *Yu et al.* [2006]. Data were processed by the ChinaFLUX CO_2 data processing system [*Li et al.*, 2008], including (1) triple coordinate rotation for 30 min flux data, (2) Webb-Pearman-Leuning (WPL) correction [*Webb et al.*, 1980], (3) abnormal data rejection [*Papale et al.*, 2006], and (4) exclusion of data from nocturnal periods when the friction velocity, $u*$, was less than a threshold calculated from the algorithm provided by *Reichstein et al.* [2005]. To fill small blocks (less than 2 h) of missing and abnormal data, a linear interpolation method was applied to each time series. Larger gaps during the daytime were filled with values derived from the Michaelis-Menten equation [*Falge et al.*, 2001]. The daytime ecosystem respiration was calculated with the Lloyd and Taylor equation [*Lloyd and Taylor*, 1994], based on observations during nighttime. GPP was finally estimated as the difference between daytime NEE and ecosystem respiration.

2.1.2. Meteorological Observations

Climate data were extracted from the daily data set produced by the China Meteorological Administration, which contain daily summaries of hourly climate data from over 700 georeferenced nationwide weather stations; 108 of these stations are located on the Tibetan Plateau (Figure 2). From this database, we extracted the daily mean air temperature, sunshine hours, and global solar radiation of the region together with their geographical coordinates. Photosynthetic active radiation (PAR) was estimated from sunshine hours and global solar radiation using the method described by *Zhu et al.* [2010]. Then the mean values of air temperature and PAR were calculated for each station at 8 day step during 2003–2008. We obtained 552 values for each station in total (2 meteorological variables × 46 periods/year × 6 years).

Thin plate spline function (ANUSPLIN) [*Hijmans et al.*, 2005; *Hutchinson and Xu*, 2013] was used to spatially interpolate observations from 108 weather stations across the Tibetan Plateau at the resolution of 1 km × 1 km. With this procedure, we created 552 maps of air temperature and PAR on the plateau.

2.1.3. Remote Sensing Data Sets

Two vegetation indices were used in this study as input data: enhanced vegetation index (EVI) and land surface water index (LSWI) [*Huete et al.*, 2002; *Xiao et al.*, 2004b]. Seven of 36 spectral bands provided by the MODIS sensor onboard the NASA Terra satellite are primarily designed for the study of vegetation and land surface. We downloaded these seven bands at 500 m resolution during 2003–2010 via the MODIS 8 day Land Surface Reflectance (MOD09A1) data sets from https://lpdaac.usgs.gov/ to generate spatial data sets of EVI and LSWI (equations (1) and (2)). For the regional application on the Tibetan Plateau, the extracted EVI and LSWI were resampled to 1 km resolution.

$$EVI = G \times (\rho_{nir} - \rho_{red}) / (\rho_{nir} + (C_1 \times \rho_{red} - C_2 \times \rho_{blue}) + L) \tag{1}$$

$$LSWI = (\rho_{nir} - \rho_{swir}) / (\rho_{nir} + \rho_{swir}) \tag{2}$$

where ρ_{nir}, ρ_{red}, ρ_{blue}, and ρ_{swir} represent the reflectance of near infrared band (NIR, 841–875 nm), red band (620–670 nm), blue band (459–478 nm), and short wave infrared band (SWIR, 1628–1652 nm), respectively. The coefficients used in the EVI algorithm are G = 2.5, C1 = 6, C2 = 7.5, and L = 1 [*Huete et al.*, 2002]. EVI includes the blue band for atmospheric correction and has been used for the study of vegetation dynamics and production [*Wu et al.*, 2010; *Xiao et al.*, 2004a, 2004b]. Additionally, to reduce the effect of cloud and capture seasonality with EVI, the original time series were smoothed with double logistic curve fit in the TIMESAT software [*Jonsson and Eklundh*, 2002, 2004]. As the SWIR band is sensitive to vegetation water content and soil moisture, a combination of NIR and SWIR bands have been used to derive water sensitive index (i.e., LSWI), which is calculated as the normalized difference between NIR and SWIR [*Xiao et al.*, 2004a, 2004b].

2.1.4. Vegetation Distribution Information

The grassland distribution on the plateau was derived from the Atlas of Grassland Resources of China with a scale of 1:1,000,000 [*The Compiling Committee of the Atlas of Grassland Resources of China*, 1993]. Fully considering the representation of ecological properties from the 10 eddy covariance tower sites across all alpine grasslands on the plateau, our work focused on alpine meadow and alpine meadow steppe. We reclassified them into four alpine grassland subtypes: alpine kobresia meadow, alpine shrub meadow, alpine

swamp meadow, and alpine meadow steppe. These subtypes account for 28.8% of the plateau, with total area of 492,000, 81,000, 81,000, and 64,000 km^2, respectively (Figure 2).

2.2. Description and Modification of VPM Model

The Vegetation Photosynthesis Model (VPM) is a LUE model developed by *Xiao et al.* [2004a, 2004b], and it assumes that vegetation canopies are composed of photosynthetically active vegetation (mostly chlorophyll, chl) and nonphotosynthetically vegetation (NPV). Thus, the fraction of photosynthetic active radiation absorbed vegetation canopy (FPAR$_{canopy}$) is partitioned into the fraction absorbed by chlorophyll (FPAR$_{chl}$) and the fraction absorbed by NPV (FPAR$_{NPV}$). Note that only the FPAR$_{chl}$ is used for photosynthesis. The function used in the VPM model for the estimation of GPP is

$$GPP = \varepsilon_g \times FPAR_{chl} \times PAR \qquad (3)$$

$$FPAR_{chl} = a \times EVI \qquad (4)$$

$$\varepsilon_g = \varepsilon_0 \times T_{scalar} \times W_{scalar} \times P_{scalar} \qquad (5)$$

where ε_g is the LUE (g C mol^{-1} PAR) and FPAR$_{chl}$ is estimated as a linear function of EVI. The VPM model uses EVI to estimate FPAR$_{chl}$, with the coefficient, a, set to be 1.0 [*Xiao et al.*, 2004a, 2004b]. The parameter ε_g is estimated as a function of the maximum LUE (ε_0) and the scalars for the effects of temperature (T_{scalar}), water (W_{scalar}), and leaf age (P_{scalar}) on LUE of vegetation [*Xiao et al.*, 2004a, 2004b].

The effect of temperature on GPP (T_{scalar}) is estimated using the equation developed for the terrestrial ecosystem model (equation (6)). In equation (6), T_{min}, T_{opt}, and T_{max} (minimal, optimal, and maximal temperature for photosynthesis, respectively) values were used to calculate T_{scalar}. Since it is unreasonable to give each biome type the same parameter value, we calculate T_{opt} of each pixel as the air temperature when the EVI in the pixel reaches the peak of the year [*Potter et al.*, 1993; *Wang et al.*, 2010]. We used 0 for T_{min} and computed T_{max} as $T_{opt} + (T_{opt} - T_{min})$ for each pixel.

$$T_{scalar} = \frac{(T - T_{min})(T - T_{max})}{[(T - T_{min})(T - T_{max})] - (T - T_{opt})^2} \qquad (6)$$

Leaf age affects the seasonal patterns of plant photosynthetic capacity and net ecosystem exchange of carbon dioxide. In this study, the period of pixel's EVI exceeding the average value of EVI was defined as the leaf full expansion period, when P_{scalar} was set as 1; for other periods, P_{scalar} was set as (1 + LSWI) / 2 [*Xiao et al.*, 2004a; *Wang et al.*, 2010].

In VPM, W_{scalar} was used to estimate the effect of land surface water conditions on photosynthesis:

$$W_{scalar} = \frac{1 + LSWI}{1 + LSWI_{max}} \qquad (7)$$

where LSWI$_{max}$ is the maximum LSWI during the growing season [*Xiao et al.*, 2004a, 2004b]. Equation (7) was proven to work well in vegetation with semihumid and humid climate [*Xiao et al.*, 2004a; *Yan et al.*, 2009]. In arid and semiarid climate, photosynthesis was more sensitive to short-term water availability. In order to simulate the rapid response, we proposed a simpler approach (equation (8)).

$$W_{scalar} = 0.5 + LSWI \qquad (8)$$

The proposed formula for W_{scalar} was similar to CASA water scalar [*Potter et al.*, 1993; *Field et al.*, 1995], with the basic difference that the ratio of estimated evapotranspiration (ET) to potential evapotranspiration (PET) was replaced with LSWI. The index was aimed to capture the rapid response of photosynthesis to water availability regardless of water condition during the whole year. Taking LSWI in HBSH during 2004 as example, the maximum LSWI was 0.355, and the slope for the original W_{scalar} was 1/(1 + LSWI$_{max}$), which equals to 0.738. For the modified version, the slope was 1, which showed higher sensitivity to short-term water fluctuations than the original formulation.

2.3. Uncertainty Analysis
2.3.1. Determination of Uncertainty in Model Parameters and Input Data
The key parameter of the VPM model, i.e., the maximum LUE (ε_0), needs to be estimated for different alpine grassland subtypes. We used Markov Chain Monte Carlo (MCMC) technique to estimate the parameters in

Michaelis-Menten light response function (equation (9)), based on NEE and PAR observation within the peak period of the vegetation growing season (from July to August) of all the available sites in each alpine grassland subtype. In equation (9), α, GEE_{max}, and R_{eco} are undetermined parameters. The maximum LUE or apparent quantum yield (g C mol^{-1} PAR) is α, GEE_{max} (μmol CO_2 m^{-2} s^{-1}) is gross ecosystem exchange of CO_2 at "saturating" light, and R_{eco} (μmol CO_2 m^{-2} s^{-1}) is ecosystem respiration. The estimated α value was used as an estimation of the ε_0 parameter in the VPM model.

$$NEE = \frac{\alpha \times PAR \times GEE_{max}}{\alpha \times PAR + GEE_{max}} - R_{eco} \tag{9}$$

Specifically, we used the Gibbs sampler implemented in JAGS (Just Another Gibbs Sampler) source code (http://mcmc-jags.sourceforge.net/) to estimate the posterior probability distributions of the parameters in light response function. The prior ranges of α, GEE_{max} and R_{eco} were specified as 0–6 g C mol^{-1} PAR, 0–100 μmol CO_2 m^{-2} s^{-1}, and 0–60 μmol CO_2 m^{-2} s^{-1}. The posterior distributions of α in each alpine grassland subtype can reflect the uncertainty on the parameter values, and the statistical characteristics (e.g., mean, standard deviation, and coefficient of variation) of the key model parameter ε_0 could be obtained.

Although it is very common to assume a fixed ε_0 value for a given alpine grassland [*Xiao et al.,* 2004a, 2004b], actually, the maximum LUE values vary not only with alpine grasslands but also within the same alpine grassland [*Xiao et al.,* 2011]. So in addition to joint-sites estimation for each alpine grassland subtype, we also employed the leave-one-out cross validation method [*Ren et al.,* 2013] to test the validity of joint estimation of the key parameter and explore how the ε_0 varies across sites within the same alpine grassland subtype. For each alpine grassland subtype that has more than one site, i.e., alpine kobresia meadow, alpine swamp meadow, and alpine meadow steppe, one site was excluded at a time and data of all other sites were used to estimate the key parameter.

Meanwhile, there are inevitable errors in gridded meteorological data sets that were generated by interpolating the meteorological station data. In this study, Bayesian standard deviation for the gridded meteorological data was provided during interpolation of the regional climate data from weather stations [*Hutchinson and Xu,* 2013]. Therefore, we considered the standard error surfaces as the uncertainty of the regional climate data.

The measurement error of remote sensing data is not easily quantified. In this study we assumed the error of satellite vegetation indices (EVI and LSWI) falls within $\pm(0.02 + 0.02*value)$ by referencing the results of several researches [*Lin et al.,* 2011; *Vermote and Kotchenova,* 2008]. Further exploration of accuracy and feasibility is needed.

2.3.2. Estimation of Uncertainty With Monte Carlo Analysis

After considering the uncertainty of maximum LUE and input data sets, we used the conceptually straightforward Monte Carlo (MC) approach to quantify the uncertainty in GPP estimation. The equations of modified VPM were repeatedly evaluated using possible model input values including ε_0, T, PAR, EVI, and LSWI, which were randomly selected from the known (or assumed) probability distributions. The probability distribution of ε_0 was obtained by the MCMC method. Uniform distributions were assumed for meteorological data (i.e., T and PAR) and satellite data (i.e., EVI and LSWI). The boundaries for individual pixels of meteorological data were obtained from the standard error surfaces, and the boundaries for satellite data were considered as (value $\pm(0.02 + 0.02*value)$) [*Lin et al.,* 2011; *Vermote and Kotchenova,* 2008]. After repeatedly initializing the modified VPM model with the perturbed model parameters and input data sets, the resultant number of predictions were used to define the probability distribution of the propagated error. In this study, the random sampling processes were repeated for a total of 1000 iterations. From the 1000 estimations for each 8 day pixel, the standard deviation (SD) of GPP estimation was calculated to represent the uncertainty of estimated GPP in the Tibetan alpine grasslands. GPP for each pixel h across the study region was computed as the average of the Monte Carlo iterations ($m = 1000$) using

$$GPP_h = \frac{1}{m} \sum_{i=1}^{m} GPP_{hi} \tag{10}$$

The relative uncertainty (RU) of the GPP estimation was expressed as two standard deviations (approximately 95% confidence interval) divided by the mean prediction value (equation (11)).

$$RU(\%) = \frac{\text{Two standard deviations}}{\text{Mean value}} \times 100 \qquad (11)$$

2.3.3. Uncertainty Partitioning Using Sobol' Variance Decomposition Method

In addition to quantify the uncertainty in GPP estimation, it is also important to understand the relative contribution of each source of uncertainty to total uncertainty and locate the most influential model input. In this study, the Sobol' variance decomposition method [*Saltelli*, 2002; *Sobol*, 1993; *Tarantola et al.*, 2006] is used to partition output uncertainty into different uncertainty sources (i.e., ε_0, T, PAR, EVI, and LSWI) for GPP simulation (equation (12)).

$$GPP = f(\varepsilon_0 \times PAR \times T \times EVI \times LSWI) \qquad (12)$$

In Sobol' method, assuming the model inputs are independent, the total variance of model output can be decomposed into components that result from individual model inputs and their interactions (equation (13)).

$$V = \sum_i V_i + \sum_i \sum_{j>i} V_{ij} + \ldots + V_{12\ldots k} \qquad (13)$$

where V is the total variance of the model output, V_i is the portion of V explained by the ith model input, $V_{i,\ldots,k}$ is the share of V explained by the interactions among the first to kth model input, and k is the total number of model inputs. Then the Sobol' sensitivity indices can be obtained by normalizing the partial variances with total output variance (equation (14)).

$$1 = \sum_i S_i + \sum_i \sum_{j>i} S_{ij} + \ldots + S_{12\ldots k} \qquad (14)$$

where S_i is the first-order sensitivity index of the ith input, representing the direct influence of a model input on the model output, and $S_{i\ldots k}$ is the kth-order sensitivity index which represents the interactions among the first to kth input. The total order sensitivity index (S_{Ti}) is the sum of all the sensitivity indices in equation (14) that include the ith input, reflecting how individual model input and its interactions with other inputs impact the model output.

For the regional application of the modified VPM model, the input data (i.e., T, PAR, EVI, and LSWI) and outputs (i.e., GPP) are all spatially distributed raster maps, not scalars, while the computation of Sobol' sensitivity indices is based on scalar inputs and outputs. So, we need to figure out how to derive spatial Sobol' indices. There are two ways to do that, including pixel-by-pixel method [*Tang et al.*, 2007] and map-labeling method [*Lilburne and Tarantola*, 2009]. In pixel-by-pixel method, we compute the Sobol' indices for each pixel respectively, since the inputs and output of each pixel are scalars. Then we can get spatial maps of Sobol' indices, denoted as map of pixel sensitivity indices. In map-labeling method, the spatial inputs are converted to scalars through numbering the random realizations of input maps and the spatial outputs are converted to scalars through setting an appropriate scalar objective function such as sum. Afterwards, we can compute the Sobol' indices for the whole study region, known as block sensitivity indices.

3. Results

3.1. Model Parameterization and Validation at the Site Level

3.1.1. Estimation and Uncertainty of Maximum LUE

The estimated values and distributions of the key parameter ε_0 from joint-sites optimization for regional GPP simulation are shown in Table 2 and Figure 3. The mean values of ε_0 vary substantially with alpine grassland subtypes, with the highest value (0.522 g C mol^{-1} PAR) occurring in alpine swamp meadow and the lowest value (0.204 g C mol^{-1} PAR) in alpine meadow steppe. The estimated values of alpine kobresia meadow and alpine shrub meadow are at an intermediate level, 0.425 g C mol^{-1} PAR and 0.443 g C mol^{-1} PAR, respectively. And the estimated distributions of ε_0 in the four alpine grassland subtypes are generally following normal distribution; only alpine meadow steppe has a slightly skewed distribution (Figure 3). This

Table 2. Joint-Sites Estimation of the Maximum LUE Parameter (ε_0) for Alpine Kobresia Meadow, Alpine Shrub Meadow, Alpine Swamp Meadow, and Alpine Meadow Steppe; and Leave-One-Out Estimation for Alpine Kobresia Meadow, Alpine Swamp Meadow, and Alpine Meadow Steppe

| | ε_0 | | | | |
Site[a]	Mean (g C mol^{-1} PAR)	Standard Deviation (g C mol^{-1} PAR)	Coefficient of Variation (%)	R^2	p
	Alpine kobresia meadow				
HBKO	0.346	0.016	4.742	0.718	<0.001
GLKO	0.460	0.014	3.038	0.561	<0.001
ARKO	0.423	0.016	3.723	0.682	<0.001
Joint sites	0.425	0.013	2.953	/	< 0.001
	Alpine Swamp Meadow				
HBSW	0.533	0.047	8.839	0.653	<0.001
DXSW	0.509	0.022	4.422	0.462	<0.001
MQSW	0.503	0.021	4.16	0.428	<0.001
Joint sites	0.522	0.021	4.092	/	<0.001
	Alpine Meadow Steppe				
DXST	0.207	0.11	53.228	0.161	<0.001
ZFST	0.184	0.041	22.126	0.231	<0.001
NMCST	0.233	0.056	24.147	0.216	<0.001
Joint sites	0.204	0.045	22.215	/	<0.001
	Alpine Shrub Meadow				
Joint sites	0.443	0.012	2.709	/	<0.001

[a]Represents one site excluded.

indicates that the ε_0 parameter can be well constrained by the observation. Meanwhile, SD and coefficient of variation (CV) of alpine meadow steppe are significantly higher than other alpine grassland subtypes.

We also conducted the leave-one-out cross validation to validate the performance of parameterization with eddy covariance data. The results showed that the ε_0 varied not only with different alpine grassland subtypes
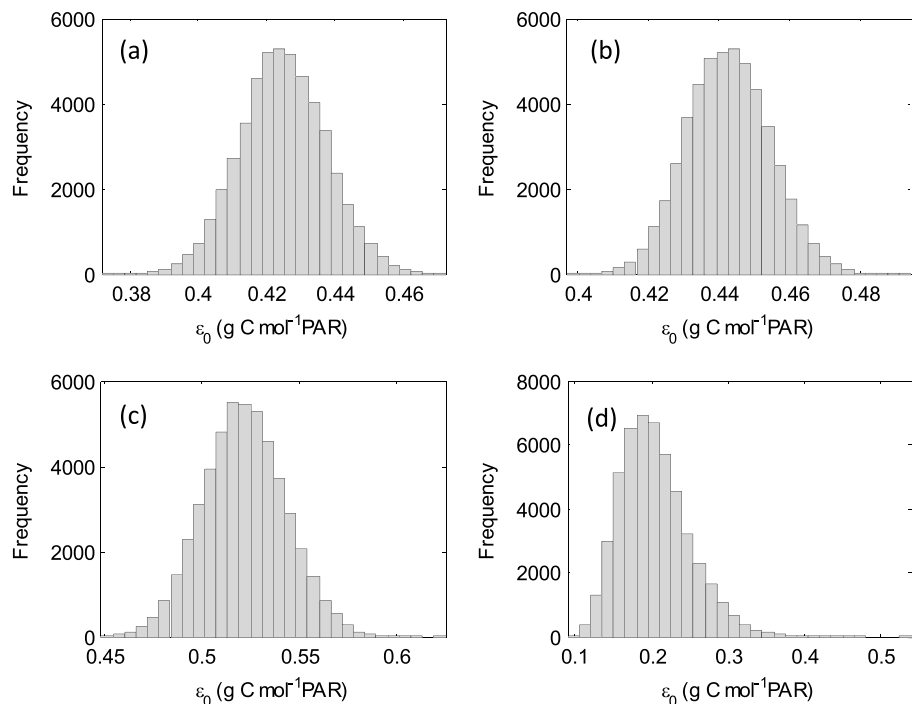

Figure 3. Probability distributions of maximum LUE (ε_0) derived from MCMC method in Tibetan alpine grasslands: (a) alpine kobresia meadow, (b) alpine shrub meadow, (c) alpine swamp meadow, and (d) Alpine meadow steppe.
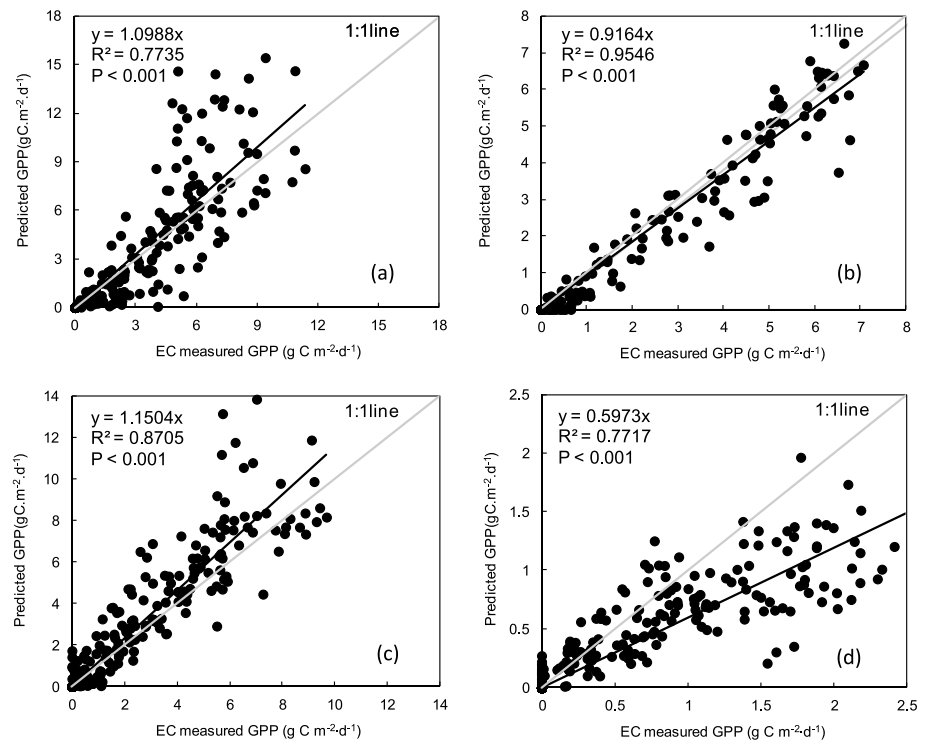
Figure 4. Comparison between the observed and predicted GPP derived from the modified VPM model in 10 EC tower sites on the Tibetan alpine grasslands: (a) alpine kobresia meadow, (b) alpine shrub meadow, (c) alpine swamp meadow, and (d) Alpine meadow steppe.

but also within the same alpine grassland subtype (Table 2); the variation of ε_0 across different sites within a given alpine grassland subtype is much smaller than that across different alpine grassland subtypes. The determination coefficient (R^2) of the cross validation for alpine kobresia meadow and alpine swamp meadow varied between 0.43 and 0.72 ($p < 0.001$), while alpine meadow steppe had a much lower R^2 varying from 0.16 to 0.23 ($p < 0.001$). We note that the estimated ε_0 with the joint-sites optimization are within the range of leave-one-out variation for a given alpine grassland subtype.

3.1.2. Model Validation at the Site Level

We computed the 8 day step GPP of the 10 sites using the estimated mean value of ε_0, based on the modified VPM model and the original version. High values of R^2 (0.77–0.95, $p < 0.001$) between GPP from flux measurement (GPP_EC) and GPP from modified VPM model (GPP_VPMm) were observed for four grassland subtypes (Figure 4).

We also compared the GPP_VPMm with GPP from original VPM (GPP_VPM), MODIS GPP product (GPP_MOD, MODIS-based GPP product [MOD17A2] downloaded from https://wist.echo.nasa.gov), and the GPP observation at the tower sites. The results were illustrated in a Taylor diagram (Figure 5). In the Taylor diagram, four statistical quantities are geometrically connected: the correlation coefficient (r), SD of observation, SD of the model, and the centered pattern root mean square [*Taylor*, 2001]. The polar axis displays the correlation coefficient and the radial axes display the root mean standard deviation (RMSD) of the modeled variable. Simulated patterns that agree well with observations will lie nearest the observed point on the x axis, having relatively high correlation and low RMSD. By integrating the consideration of r and RMSD, as shown in Figure 5, we note that the GPP_VPMm provides a better agreement than the GPP_VPM and GPP_MOD. Most notably, an obvious improvement in model performance with the modified VPM model is observed in the alpine meadow steppe. The original W_{scalar} in the VPM is insufficiently sensitive to water stress in dry land, and the modified W_{scalar} clearly improved the model's capacity to reproduce summer 8 day productivity.

3.2. Regional GPP and Uncertainties

We calculated annual GPP for each year during 2003–2008 from the 8 day GPP estimates. The total annual GPP for the studied area and for each subtype of alpine grassland over the period was shown in Table 3 and
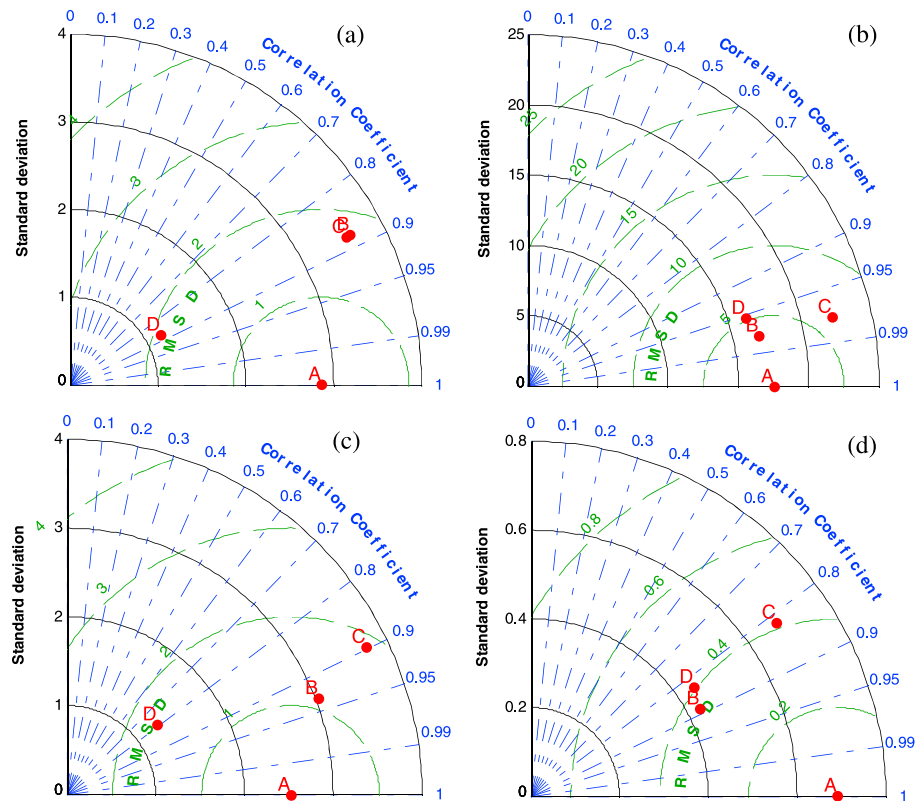
Figure 5. Performance of modified VPM (letter B), VPM (letter C), and MODIS (letter D) product in GPP estimation at 10 flux sites during the study period. Letter A on the *x* axis means the observed value.

Figure 6. On average, the total annual GPP was 223.3 Tg C yr^{-1}, with 4.6 Tg C yr^{-1} for alpine meadow steppe and 154.8 Tg C yr^{-1} for alpine kobresia meadow. In our 6 year estimate, the carbon uptakes were the lowest and highest in 2008 and 2006, with 212.8 and 233.7 Tg C yr^{-1}, respectively. The regional simulations indicate that there is large spatial variability in the capacity of carbon fixation in the region (Figure 7a), which corresponds well with the spatial variations in climate and biophysical properties. To examine how the climate gradients affected GPP, we selected an east-west transect along the latitude 30°–35°N and a south-north transect along the longitude of 95°–100°E (Table 4). The result shows that GPP on the plateau grassland followed a clear longitudinal gradient, increasing from west to east, attributable primarily to the increase of precipitation, air temperature, and the decrease in elevation, while the decrease of GPP from south to north is primarily controlled by air temperature.

To further analyze the interannual variations of regional GPP, we calculated the interannual variability (IAV) for each pixel (Figure 7b), defined as the coefficient of variation of the quantity of GPP in each pixel across all years. There are evident interannual variations in most areas, and the average IAV for all pixels is 15%. The highest interannual variation of GPP occurred in the middle part of the plateau, with the values larger than

Table 3. Annual GPP Estimations for Four Alpine Grassland Subtypes on the Tibetan Plateau during 2003–2008[a]

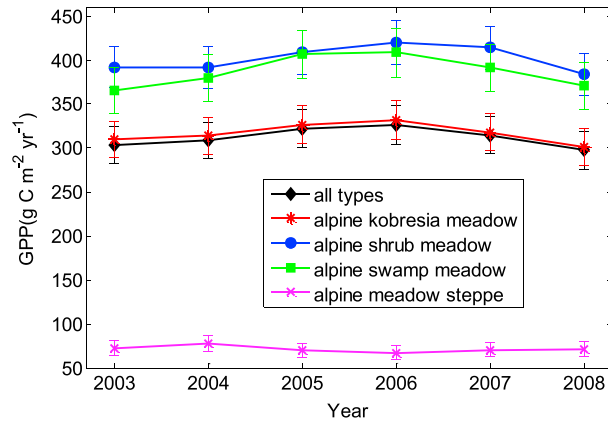| Alpine Grassland Subtype	2003	2004	2005	2006	2007	2008	Mean
Alpine kobresia meadow	151.2	153.5	159.7	162.3	155.2	147.1	154.8
Alpine shrub meadow	31.9	31.9	33.4	34.2	33.8	31.3	32.7
Alpine swamp meadow	29.3	30.4	32.7	32.8	31.4	29.8	31.1
Alpine meadow steppe	4.7	5.1	4.5	4.4	4.6	4.6	4.6
Total	217.2	220.9	230.3	233.7	225.0	212.8	223.3

[a]Unit: Tg C yr^{-1}.

Figure 6. Annual GPP estimations and standard deviations for four alpine grassland subtypes on the Tibetan Plateau during 2003–2008. Unit: g C m^{-2} yr^{-1}.

25%. From Figure 8, we can see that the seasonal variations of regional GPP are also distinct on the plateau, with the significantly larger amplitude of GPP occurring in the growing season (Figure 8a) than the whole year (Figure 8b). The seasonal cycle of EVI seams to dominate the seasonal variations of GPP in most areas, since the seasonal variations of GPP are most strongly correlated with the seasonal cycle of EVI across 88% of the study area (Figure 8c). The seasonal variation of temperature is strongly associated with that of GPP in about 11% of the study area, mostly distributed in the regions with small amplitude of GPP (Figure 8c).

We compared the regional estimates of GPP derived from the modified VPM (GPP_VPMm) and the MODIS-PSN model used for the MODIS GPP data product (GPP_MOD, MOD17A2) (downloaded from https://wist.echo.nasa.gov/) (Figure 9). The spatial patterns of our
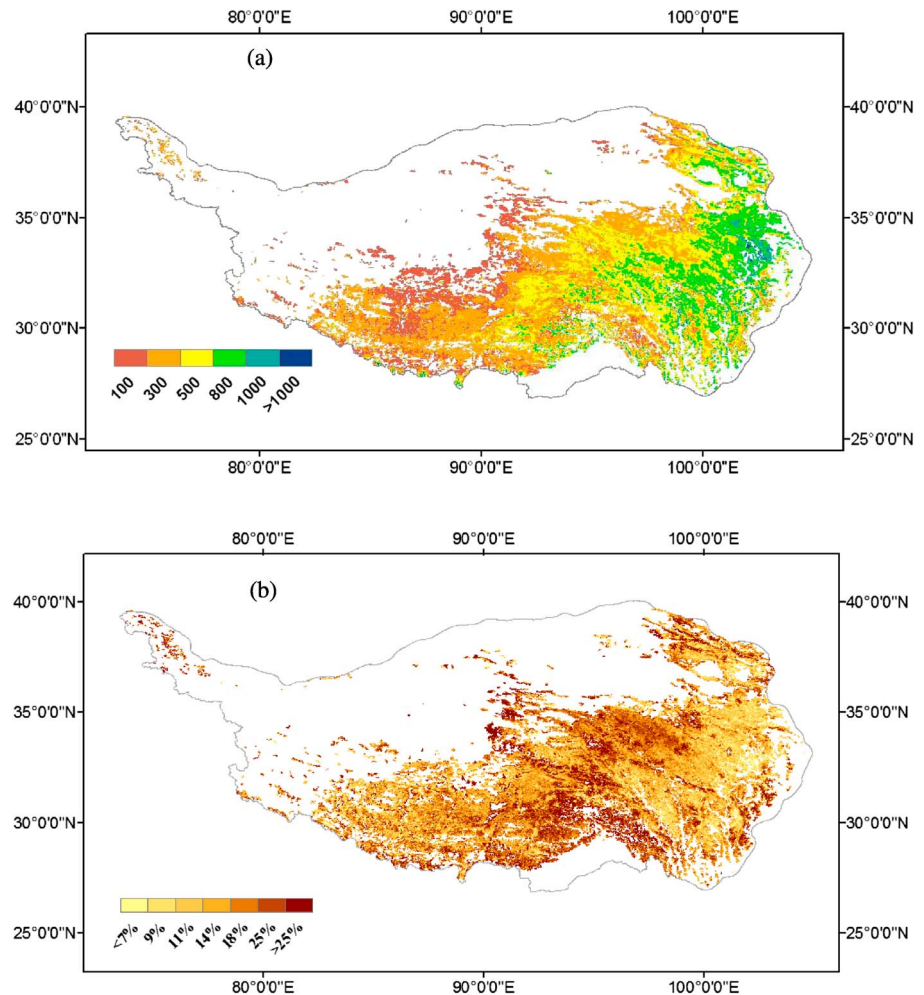

Figure 7. Spatial patterns of (a) annual GPP and (b) its interannual variation (IAV) in Tibetan alpine grasslands from 2003 to 2008. The GPP values were simulated with the modified VPM (unit: g C m^{-2} yr^{-1}).

Table 4. Pearson Correlation Matrix (P<0.05) for GPP and Environmental Variables in the East-West Transect (EWT, Along the Latitude 30–35°N, Shown in the Upper Triangle) and the South-North Transect (SNT, Along the 95–100°E, Shown in the Lower Triangle) on the Tibetan Alpine Grasslands

	EWT				
SNT	GPP	Longitude	Elevation	Air Temperature	Precipitation
GPP	1	0.68	−0.76	0.37	0.48
Latitude	−0.26	1	−0.79	−0.07	0.58
Elevation	−0.38	−0.14	1	−0.39	−0.32
Air temperature	0.54	−0.74	−0.43	1	0.21
Precipitation	0.17	−0.84	0.08	0.60	1

estimate and GPP_MOD were generally similar to each other. Both estimates of VPMm and MODIS-PSN capture the spatial patterns of GPP in the Tibetan alpine grasslands. However, the differences between the GPP_VPMm and GPP_MOD at the regional scale are due to the following two aspects. (1) GPP_VPMm presented much clearer spatial continuity, i.e., the values of GPP-VPMm gradually decreases from east to west in general, following the gradients of air temperature and vegetation cover. By contrast, the spatial pattern of GPP_MOD is not so obvious. (2) GPP_VPMm provides a higher GPP estimation for the study region than that obtained from the PSN algorithm. GPP_VPMm ranges from 0 to 1367.1 g C m^{-2} yr^{-1} with an average value of 312.3 ± 198.2 g C m^{-2} yr^{-1}, whereas GPP_MOD ranges from 0 to 1479.2 g C m^{-2} yr^{-1} with an average value of 157.6 ± 115.4 g C m^{-2} yr^{-1}. The difference between these two results increases with the increasing magnitude of GPP, and it is highest in east-central part of the study region.

The uncertainty of GPP derived with modified VPM for the Tibetan alpine grasslands with MC approach was presented in Figure 10. The spatial pattern of estimated SD is similar to that of GPP (see Figure 7a), with higher values in eastern region (more than 35 g C m^{-2} yr^{-1}) and lower values in the western part of the plateau. The average SD of the GPP estimation in Tibetan alpine grasslands is 20.7 g C m^{-2} yr^{-1}. Roughly 75% of grassland has a SD of 10–30 g C m^{-2} yr^{-1}, with GPP estimation ranging from 13.5 to 763.0 g C m^{-2} yr^{-1}. In addition, the minimum value of mean RU in the study area is about 6.9%, and most of RU ranges from 10% to 30%, with the largest uncertainty occurring in regions with lower GPP. RU originated from the model parameters, and input data sets for the annual GPP at regional scale was ranging from 6.9% to 34.6%, averaged at 18.3%, which is much larger than the global uncertainty estimate (9.86%) of *Jung et al.* [2011]. Such a difference is likely because of the difference of study regions, Tibetan alpine grasslands versus all vegetation types of the globe. Moreover, as shown in Figures 10 and 11, the spatial distribution of RU, SD of air temperature, and PAR are rather similar to each other. In the northwest of the plateau, the number of the weather stations is limited (see Figure 2), resulting in a high uncertainty for the gridded climate data that is propagated to the estimated GPP.

3.3. Uncertainty Partitioning of the Modeled GPP

We conducted the map-labeling Sobol' analysis in several 8 day steps covering different phases of the growing season of the alpine grasslands, including DOY 161–168, 185–192, 209–216, and 233–240 in the year 2004, and found that the ranking of model inputs for uncertainty contribution is identical across different time steps, although the specific values of uncertainty contribution are slightly different. So we chose one 8 day time step (DOY 209–216) to illustrate the relative contribution of each source of uncertainty to the total uncertainty. The block sensitivity indices results presented in Table 5 showed that the sequence of relative importance is: PAR > EVI > ε_0 > T ≈ LSWI. More than 85% of uncertainty in estimated GPP is contributed to the maximum LUE, PAR, and EVI, while T and LSWI only contributed about 15%. This indicated that maximum LUE, PAR, and EVI have much greater influence on estimated GPP than T and LSWI. Furthermore, the sum of first-order sensitivity indices and the sum of total order sensitivity indices are 99.51% and 101.07%, respectively (Table 5), with very small difference, reflecting that the influence of the parameters themselves dominates their overall uncertainty contribution rather than the interactions with other variables.

The map of pixel sensitivity indices was also analyzed for one 8 day time step (DOY 209–216) and used to further analyze the spatial distributions of relative importance of each input variable. Figure 12 illustrated the spatial distribution of total order sensitivity indices for each input variable. Due to the heterogeneous spatial distributions of RU of each variable (Figure 13), the spatial patterns of uncertainty contribution of each input
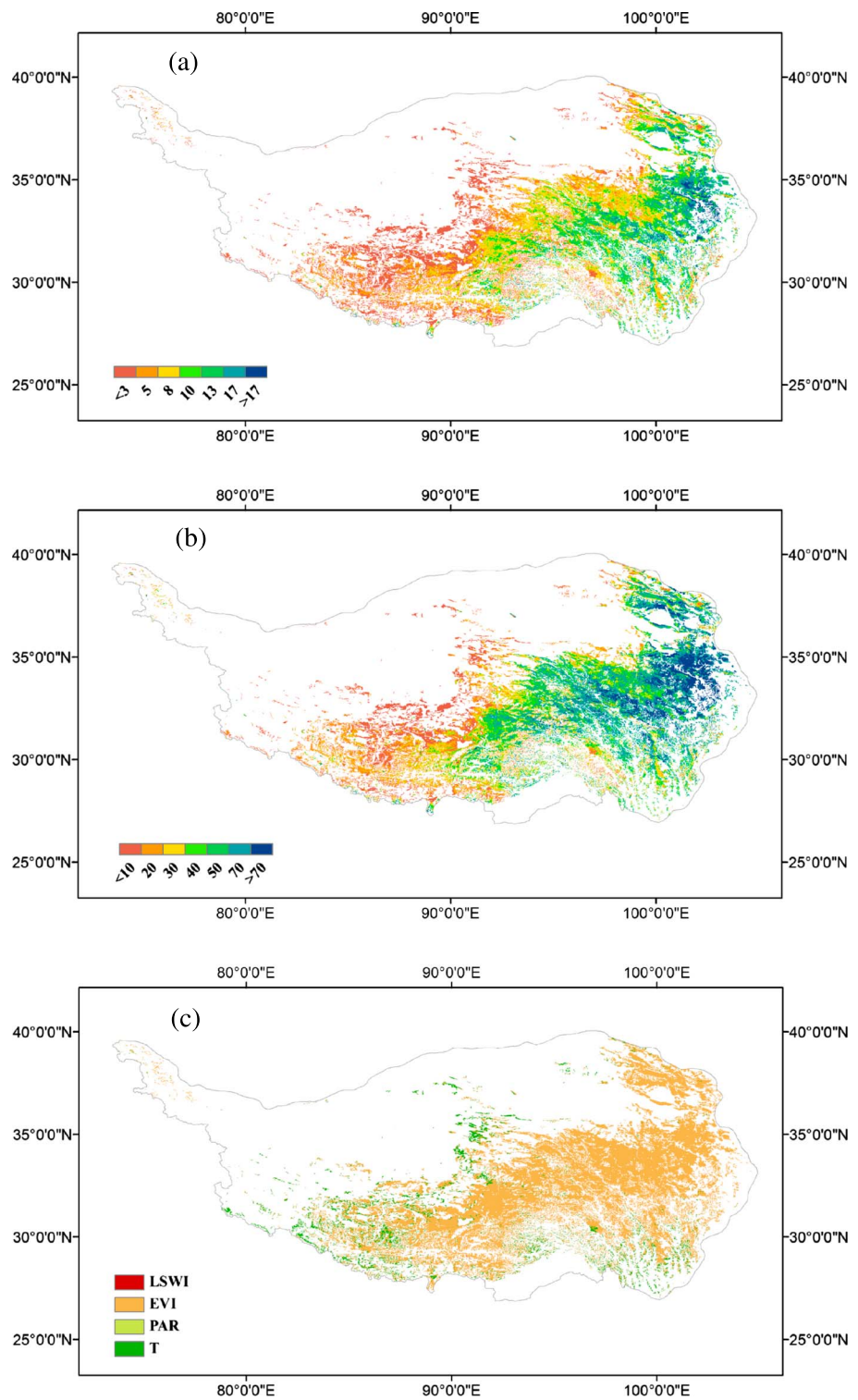
Figure 8. The regional map of the mean seasonal cycle of modeled GPP from 2003 to 2008 and the corresponding environmental variable with the maximum correlation coefficient. (a) The amplitude of the mean seasonal cycle of GPP during 2003–2008(unit: $g\,C\,m^{-2}\,8d^{-1}$), (b) the maximum 8 day flux of the mean seasonal cycle of GPP(unit: $g\,C\,m^{-2}\,8d^{-1}$), and (c) the maximum value composite of correlation coefficient between modeled GPP and environmental variables, i.e., T, PAR, EVI, and LSWI.
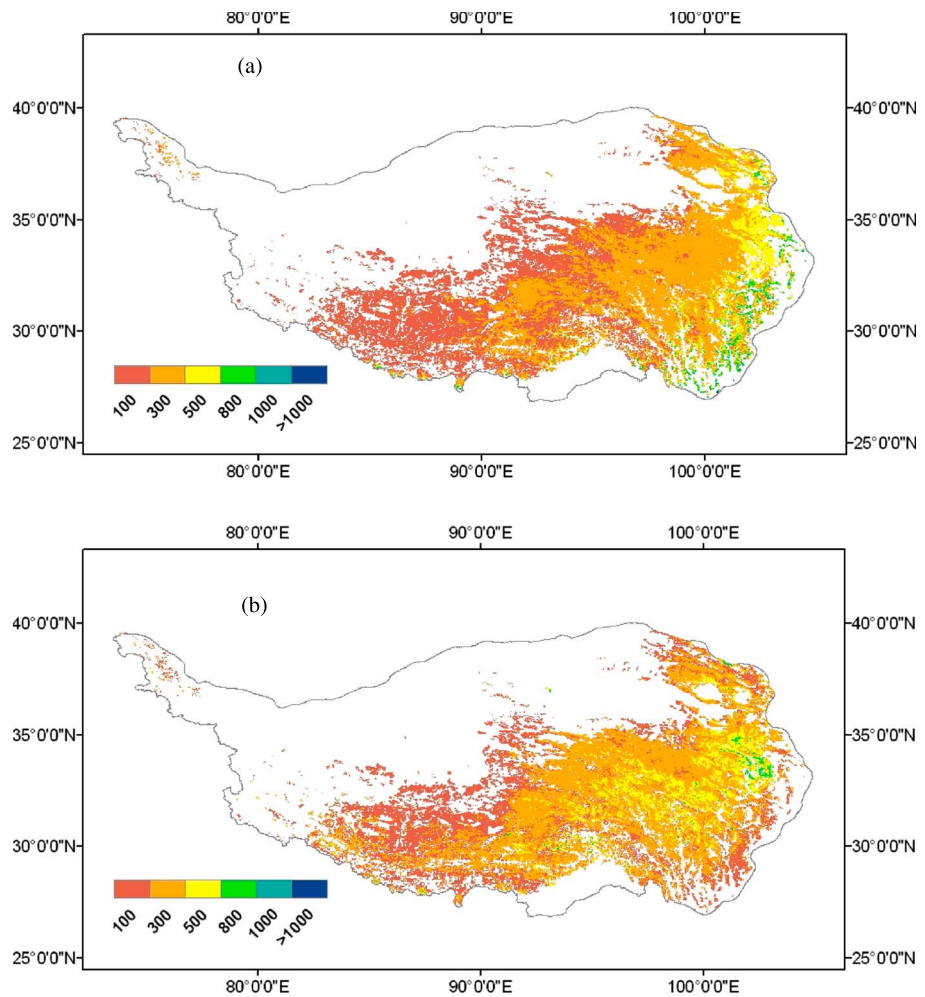
Figure 9. The comparison of grassland annual GPP images of GPP_VPMm and (a) GPP_MOD, and (b) the difference between GPP_VPMm and GPP_MOD in alpine grasslands on the Tibetan Plateau.

variable are inhomogeneous across the region (Figure 12). For ε_0, the spatial distribution of total order indices is similar to the alpine grassland classification map in Figure 2, and alpine meadow steppe and alpine swamp meadow have higher uncertainty contribution than alpine shrub meadow and alpine kobresia meadow. For T and LSWI, the uncertainty contribution is higher in the eastern than the western part of the plateau. For EVI, the eastern and middle parts of the plateau have the lowest uncertainty contribution. For PAR, the uncertainty contribution of the southern part of the plateau to estimated GPP is much higher than the northern part.

4. Discussion

4.1. Maximum LUE and Its Influence on Model Estimation

The determination of maximum LUE, indicating the potential conversion efficiency of absorbed PAR under the ideal growing condition, has been recognized as very important in GPP simulation with satellite-driven LUE models in earlier studies [*Xiao et al.*, 2004b, 2011]. The maximum LUE was assumed a universal invariant across plant function types (PFTs) in some previous models [*Potter et al.*, 1993]. Meanwhile, PFT-dependent maximum LUE parameterization scheme was also found in many recent studies [*Running et al.*, 2000; *Xiao et al.*, 2004a, 2004b], with a fixed maximum LUE for a given PFT. In terms of grassland, the reported maximum LUE showed considerable variation among existing studies. The maximum LUE for global data set was demonstrated as
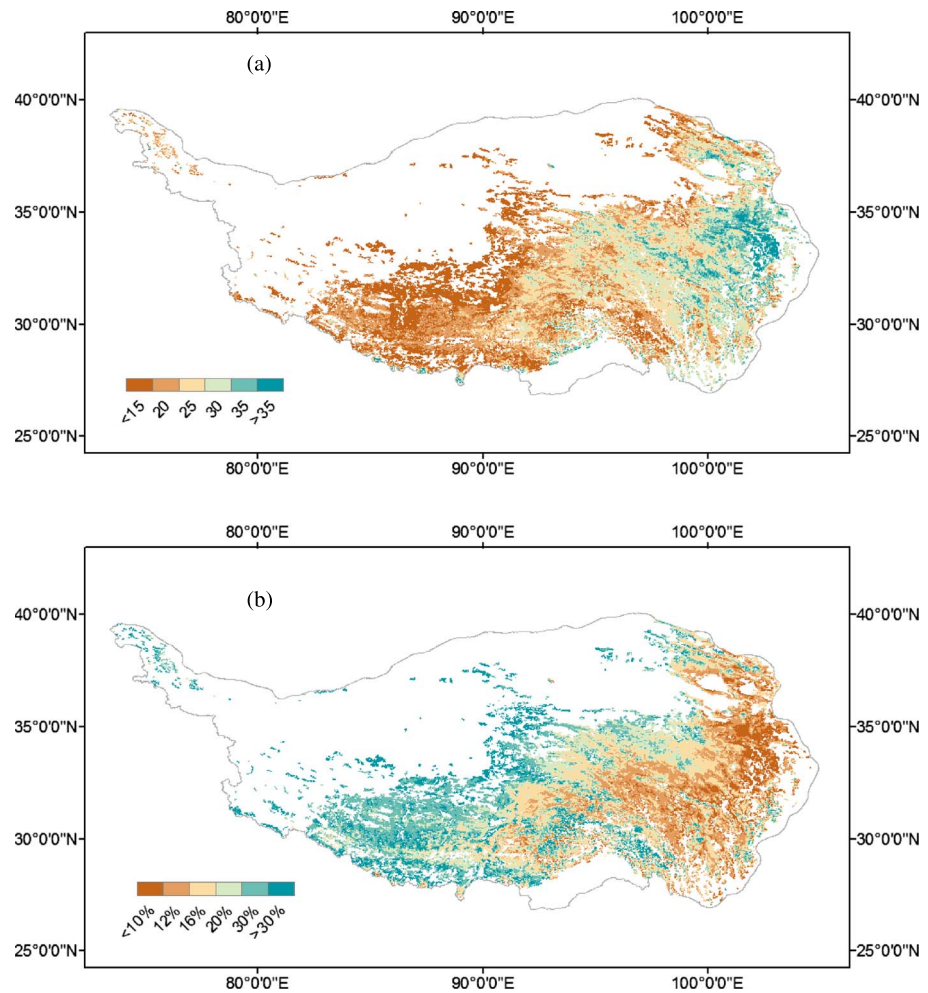
Figure 10. Uncertainty of GPP estimation in Tibetan alpine grasslands during the period of 2003–2008: (a) standard deviation of the estimation with units of g C m^{-2} yr^{-1} and (b) relative uncertainty of GPP estimation.

1.0–3.5 g C MJ^{-1} PAR (i.e., 0.21–0.76 g C mol^{-1} PAR) in *Garbulsky et al.* [2010]. An even larger variation was found in European grasslands, with a mean maximum LUE value 2.09 g CO_2 mol^{-1} PAR (0.57 g C mol^{-1} PAR) and varies in the broad range from 0.7 g CO_2 mol^{-1} PAR (0.19 g C mol^{-1} PAR) in a dry seminatural grassland to 3.3 g CO_2 mol^{-1} PAR (0.90 g C mol^{-1} PAR) in an intensive managed grassland [*Gilmanov et al.,* 2007]. For the grasslands in northern China, the maximum LUE ranged from 0.16 to 0.47 g C mol^{-1} PAR [*Wang et al.,* 2010].

The large within-PFT variability of the maximum LUE indicates that it is inadequate to use data from a single site to extract the parameters of a given PFT for regional applications. Our study showed that the maximum LUE exhibits considerable variation from 0.204 to 0.522 g C mol^{-1} PAR across four alpine grassland subtypes. Even within the same alpine grassland subtype (e.g., alpine kobresia meadow, HBKO, GLKO, and ARKO), the maximum LUE ranges from 0.346 to 0.460 g C mol^{-1} PAR, which also showed that the maximum LUE optimized from a single site does not cover the full range of variability of parameter values within a given alpine grassland subtype. The traditional parameter estimation approach may not capture the variability of ecological properties within a PFT and could bring biases to the resulting regional carbon flux estimates. Ideally, observations from multiple sites as much should be used for parameter estimation for a given PFT. In our study, the overall regional GPP estimation based on joint-sites optimization were close to the results based on leave-one-out model optimization, showing that the maximum LUE based on joint-sites optimization can lead to more robust carbon flux estimation and reduce the uncertainty in regional GPP estimation.
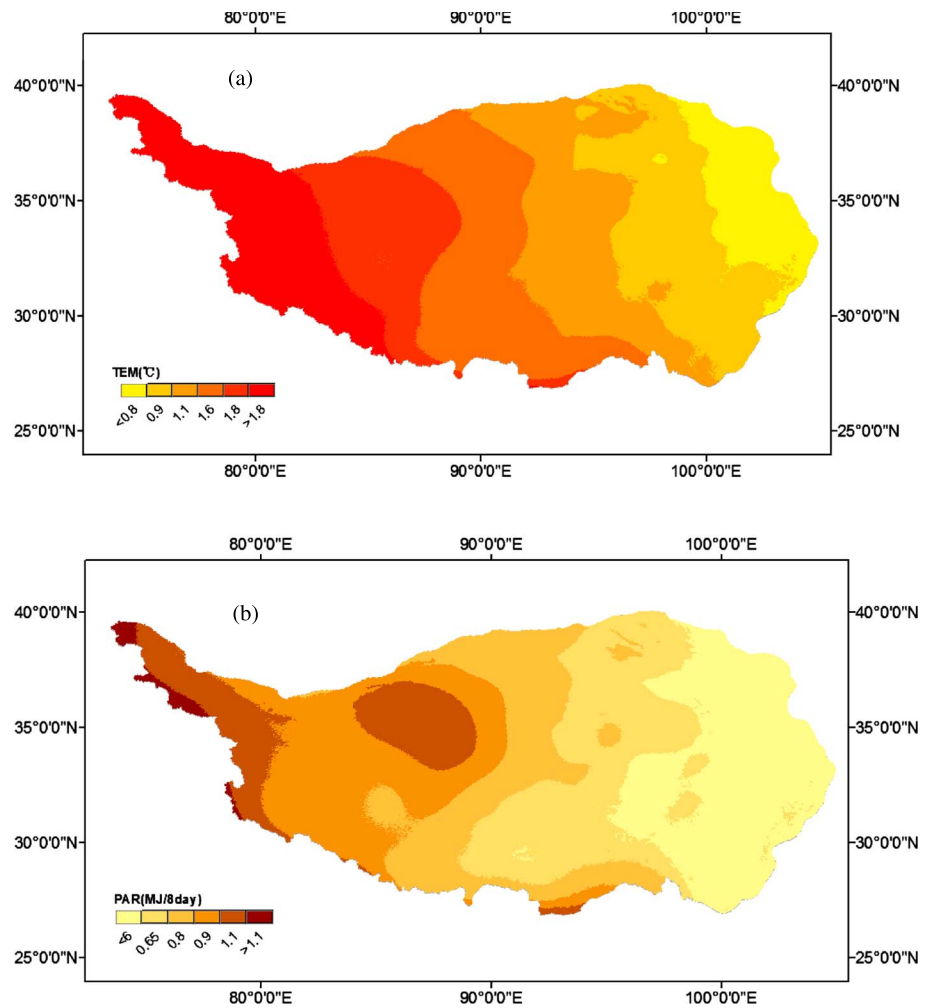
Figure 11. The standard deviation of meteorological data derived from ANUSPLIN interpolation: (a) air temperature and (b) photosynthetic active radiation.

Although differences exist in model algorithm and input data, the discrepancy in GPP estimation between VPMm and the MODIS-PSN algorithm is mainly attributed to the determination of the maximum LUE. The PSN assumes one ε_0 value per biome type [*Running et al.*, 2000] and uses a value of 0.00068 Kg C MJ^{-1} PAR [*Heinsch et al.*, 2003], i.e., 0.148 g C mol^{-1} PAR (where 1 MJ PAR is equal to ~4.6 mol PAR) for grassland. This value is much smaller than the values (0.204 to 0.522 g C mol^{-1} PAR) we obtained from eddy covariance towers in this study. *Zhang et al.* [2008] pointed out that the maximum LUE in the PSN algorithm was underestimated for the meadow, which may be the largest uncertainty of GPP_MOD [*Wu et al.*, 2010].

Table 5. The Sobol' Sensitivity Indices of Model Inputs of Modified VPM on the Tibetan Plateau (Take DOY 209–216, 2004 as Example), Estimated Using Spatial Version of Sobol' Variance Decomposition Method

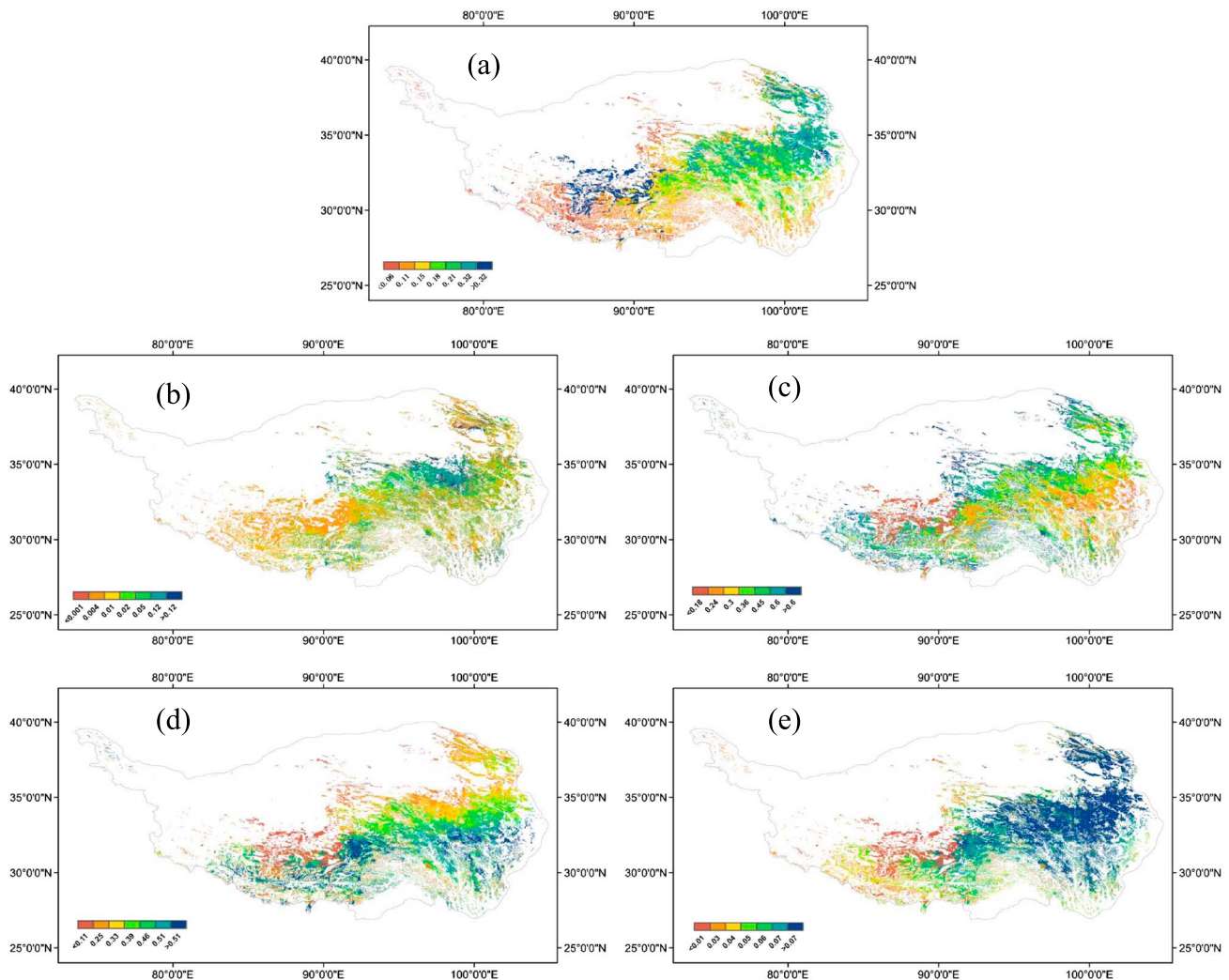| Input Variables	First-Order Sensitivity Index (S_i)	Total Order Sensitivity Index (S_{Ti})
ε_0	0.21812	0.21988
T	0.07025	0.08009
PAR	0.36756	0.36843
EVI	0.26846	0.26862
LSWI	0.07072	0.07369
Sum	0.99511	1.01071

Figure 12. The total order sensitivity indices of (a) ε0, (b) T, (c) EVI, (d) PAR, and (e) LSWI (take DOY 209–216, 2004 as example), estimated using Sobol' variance decomposition method pixel by pixel.

4.2. Uncertainty Analysis in GPP Estimations

The uncertainty in GPP simulation results from a combination of conceptual and functional model attributes such as model structure, data inputs, and model parameters [*Verstraeten et al.*, 2008]. In this study, with the consideration of the rapid response of plant photosynthesis to short-term water availability, we modified the model structure and improved the model performance in simulating GPP in four alpine grasslands ($R^2 = 0.82$–0.96, $p < 0.001$), especially alpine meadow steppe (Figure 5). By modifying model structure and validating model simulation against observation, it is possible to reduce the uncertainty caused by model structure.

The Sobol' analysis in this study showed how the overall model output uncertainty can be partitioned into contributions from different model inputs. This uncertainty partitioning reflected not only the model sensitivity but also the uncertainty of model inputs. If the model is very sensitive to an input but this input has very small uncertainty, then the uncertainty contribution of this input might be small, and vice versa. To further explore the reasons for the uncertainty contribution ranking of block sensitivity indices, i.e., $PAR > EVI > \varepsilon_0 > T \approx LSWI$, we performed one-at-a-time (OAT) local sensitivity analysis on the modified VPM model. The OAT sensitivity ranking is $PAR = EVI = \varepsilon_0 > T >> LSWI$. This implied that estimated GPP is more sensitive to maximum LUE, PAR, and EVI than air temperature, and much less sensitive to LSWI than air temperature. This is clearly due to the model structure of the modified VPM model. Although the OAT
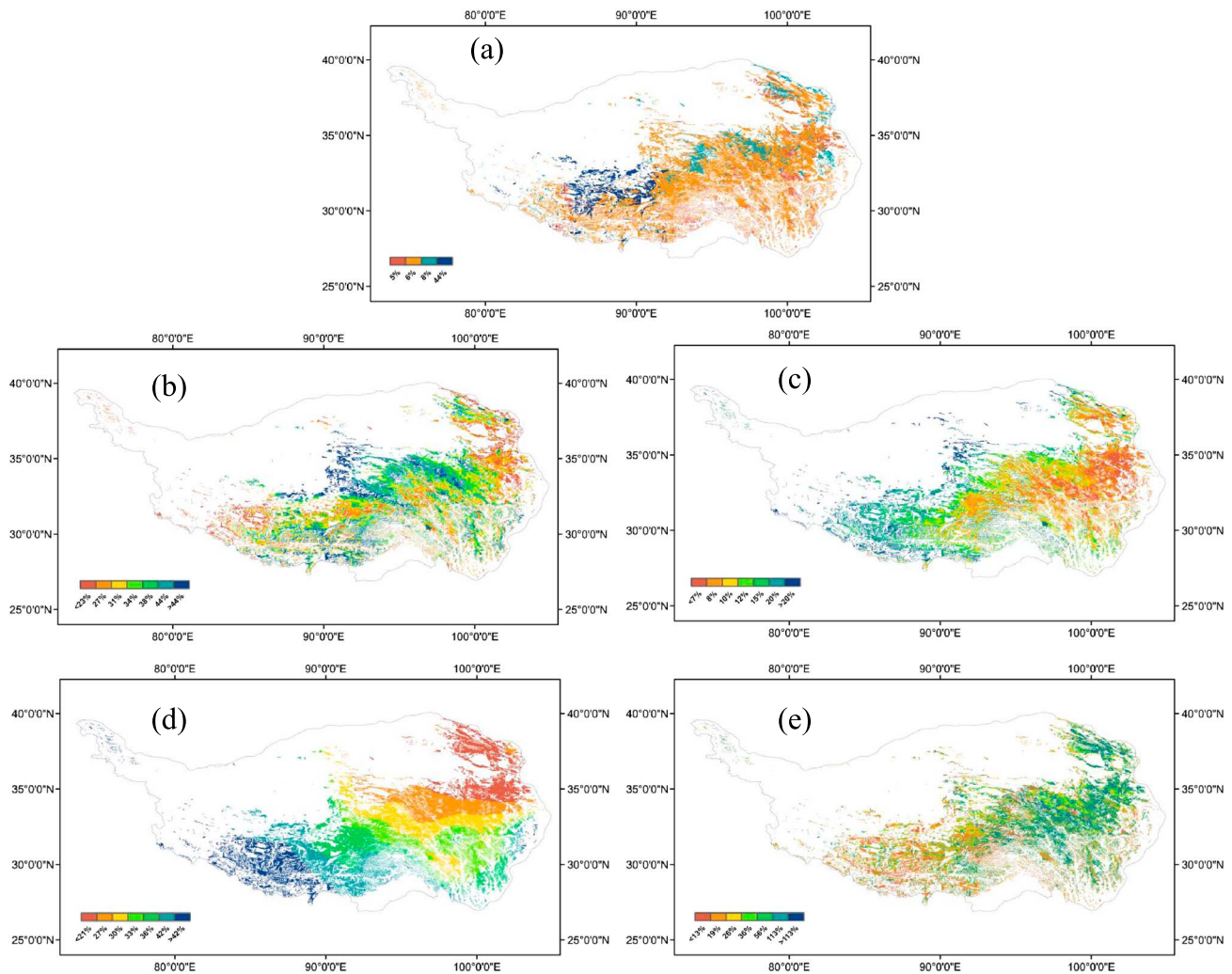
Figure 13. The relative uncertainty of (a) ε_0, (b) T, (c) EVI, (d)PAR, and (e) LSWI.

sensitivity of PAR, EVI, and ε_0 are the same, their Sobol' uncertainty contributions are different. This may be attributable to the ranking of RU of these variables, i.e., PAR (16.16%) > EVI (6.40%) > ε_0 (4.92%). In addition, we note that the OAT sensitivity of air temperature is much larger than LSWI, while the uncertainty contributions are almost the same. This is likely because the RU of LSWI (26.42%) is much larger than that of air temperature (16.97%).

As for the spatial distribution characteristics of uncertainty contribution of each input variable derived from pixel-by-pixel Sobol' method, the RU of each input variable is the key factor. Figure 13 illustrated the spatial distributions of RU of each input variable, and in combination with Figure 12, we can see that where there is a large parameter uncertainty, there is a large uncertainty contribution; i.e., the spatial distributions of RU and uncertainty contribution for each input variable are roughly similar. The minor differences between them may be attributed to the interactions between input variables. Taking DXST and HBKO for example, the RU of ε_0 in DXST is 44.12%, larger than the value 6.12% in HBKO, and the total order sensitivity index in DXST is also larger than that of HBKO, 87% versus 25%. Similarly, the RU of LSWI in DXST is 21.21%, smaller than the value 28.79% in HBKO, and the total order sensitivity index in DXST (1%) is also smaller than that of HBKO (11%).

Overall, a comprehensive analysis of the uncertainty of model output is still a big challenge for carbon cycle research. This paper tried to quantify and partition the uncertainty of estimated GPP in Tibetan alpine grasslands for the purpose of reducing the uncertainty in the future, and the main findings are that the

uncertainty of estimated GPP is 18.3% and PAR, EVI, and the maximum LUE are the main uncertainty sources. While the maximum LUE is generally thought as the most important uncertainty source of regional GPP estimation based on LUE model [*Lin et al.*, 2011], the results of this study imply that reducing the uncertainty in the driving variables of the LUE model is also very important in the regional simulation with LUE model.

5. Conclusions

With integration of CO_2 flux observation, climate, and remote sensing data, we used the modified VPM, a LUE model, to examine the magnitude, spatial pattern, and interannual variability of GPP in Tibetan alpine grasslands. Our results show that the modified model was able to reproduce the magnitude and the temporal dynamics of the carbon fixation on the plateau. The modeling results indicate that the mean annual GPP for Tibetan alpine grasslands from 2003 to 2008 was estimated at 223.3 Tg C yr^{-1} (312.3 g C m^{-2} yr^{-1}), ranging from 212.8 Tg C yr^{-1} (297.7 g C m^{-2} yr^{-1}) in 2008 to 233.7 Tg C yr^{-1} (326.9 g C m^{-2} yr^{-1}) in 2006. Our simulation also indicates that the regional GPP exhibited a large spatial variability due to changes in temperature, precipitation, and vegetation distribution. The relative uncertainty of the estimation caused by the impact of errors in model parameters and input data sets for the whole region was estimated as 18.3%, with a SD of 20.68 g C m^{-2} yr^{-1}. PAR, EVI, and the maximum LUE contributed 36.84%, 26.86%, and 21.99% of the uncertainty in estimated GPP, respectively, while T and LSWI only contributed 8.01% and 7.37%, respectively. It is clear that reducing the uncertainty in PAR and EVI is also important in the regional GPP estimation using LUE model, probably even more important than the maximum LUE.

References

Aber, J. D., P. B. Reich, and M. L. Goulden (1996), Extrapolating leaf CO2 exchange to the canopy: A generalized model of forest photosynthesis compared with measurements by eddy correlation, *Oecologia*, *106*(2), 257–265.

Beer, C., M. Reichstein, P. Ciais, G. D. Farquhar, and D. Papale (2007), Mean annual GPP of Europe derived from its water balance, *Geophys. Res. Lett.*, *34*, L05401, doi:10.1029/2006GL029006.

Beer, C., et al. (2010), Terrestrial gross carbon dioxide uptake: Global distribution and covariation with climate, *Science*, *329*(5993), 834–838.

Beven, K. (1989), Changing ideas in hydrology—The case of physically-based models, *J. Hydrol.*, *105*(1–2), 157–172.

Beven, K. (2006), A manifesto for the equifinality thesis, *J. Hydrol.*, *320*(1–2), 18–36.

Beven, K., and J. Freer (2001), Equifinality, data assimilation, and uncertainty estimation in mechanistic modelling of complex environmental systems using the GLUE methodology, *J. Hydrol.*, *249*(1–4), 11–29.

Canadell, J. G., et al. (2000), Carbon metabolism of the terrestrial biosphere: A multitechnique approach for improved understanding, *Ecosystems*, *3*(2), 115–130.

Cao, M. K., and F. I. Woodward (1998), Net primary and ecosystem production and carbon stocks of terrestrial ecosystems and their responses to climate change, *Global Change Biol.*, *4*(2), 185–198.

Davis, K. J., P. S. Bakwin, C. Yi, B. W. Berger, C. Zhao, R. M. Teclaw, and J. G. Isebrands (2003), The annual cycles of CO_2 and H_2O exchange over a northern mixed forest as observed from a very tall tower, *Global Change Biol.*, *9*, 1278–1293, doi:10.1046/j.1365-2486.2003.00672.x.

Denman, K. L., et al. (2007), Couplings between changes in the climate system and biogeochemistry, in *Climate Change 2007: The Physical Science Basis. Contribution of Working Group I to the Fourth Assessment Report of the Intergovernmental Panel on Climate Change*, edited by S. Solomon et al., pp. 499–587, Cambridge Univ. Press, Cambridge, U. K. and New York.

Desai, A. R., et al. (2008), Cross-site evaluation of eddy covariance GPP and RE decomposition techniques, *Agric. For. Meteorol.*, *148*(6–7), 821–838.

Falge, E., et al. (2001), Gap filling strategies for long term energy flux data sets, *Agric. For. Meteorol.*, *107*(1), 71–77.

Falge, E., et al. (2002a), Seasonality of ecosystem respiration and gross primary production as derived from FLUXNET measurements, *Agric. For. Meteorol.*, *113*(1–4), 53–74.

Falge, E., et al. (2002b), Phase and amplitude of ecosystem carbon release and uptake potentials as derived from FLUXNET measurements, *Agric. For. Meteorol.*, *113*(1–4), 75–95.

Field, C. B., J. T. Randerson, and C. M. Malmström (1995), Global net primary production: Combining ecology and remote sensing, *Remote Sens. Environ.*, *51*(1), 74–88, doi:10.1016/0034-4257(94)00066-V.

Garbulsky, M. F., J. Peñuelas, D. Papale, J. Ardö, M. L. Goulden, G. Kiely, A. D. Richardson, E. Rotenberg, E. M. Veenendaal, and I. Filella (2010), Patterns and controls of the variability of radiation use efficiency and primary productivity across terrestrial ecosystems, *Global Ecol. Biogeogr.*, *19*, 253–267.

Gilmanov, T. G., et al. (2007), Partitioning European grassland net ecosystem CO_2 exchange into gross primary productivity and ecosystem respiration using light response function analysis, *Agric. Ecosyst. Environ.*, *121*(1–2), 93–120.

Groenendijk, M., et al. (2011), Assessing parameter variability in a photosynthesis model within and between plant functional types using global Fluxnet eddy covariance data, *Agric. For. Meteorol.*, *151*(1), 22–38.

Haan, C. T. (1989), Parametric uncertainty in hydrologic modeling, *Trans. ASABE*, *32*(1), 137–146.

Heinsch, F. A., et al. (2003), User's guide GPP and NPP(MOD17A2/A3) products NASA MODIS land algorithm. [Available at http://www.ntsg. umt.edu/sites/ntsg.umt.edu/files/modis/MOD17 UsersGuide.pdf.]

Hijmans, R. J., S. E. Cameron, J. L. Parra, P. G. Jones, and A. Jarvis (2005), Very high resolution interpolated climate surfaces for global land areas, *Int. J. Climatol.*, *25*(15), 1965–1978.

Huete, A., K. Didan, T. Miura, E. P. Rodriguez, X. Gao, and L. G. Ferreira (2002), Overview of the radiometric and biophysical performance of the MODIS vegetation indices, *Remote Sens. Environ.*, *83*(1–2), 195–213.

Hutchinson, M. F., and T. B. Xu (2013), ANUSPLIN Version 4.4 User Guide. [Available at http://fennerschool.anu.edu.au/files/anusplin44.pdf.]

Jonsson, P., and L. Eklundh (2002), Seasonality extraction by function fitting to time-series of satellite sensor data, *IEEE Trans. Geosci. Remote Sens.*, *40*(8), 1824–1832.

Jonsson, P., and L. Eklundh (2004), TIMESAT—A program for analyzing time-series of satellite sensor data, *Comput. Geosci.*, *30*(8), 833–845.

Jung, M., M. Verstraete, N. Gobron, M. Reichstein, D. Papale, A. Bondeau, M. Robustelli, and B. Pinty (2008), Diagnostic assessment of European gross primary production, *Global Change Biol.*, *14*(10), 2349–2364.

Jung, M., et al. (2011), Global patterns of land-atmosphere fluxes of carbon dioxide, latent heat, and sensible heat derived from eddy covariance, satellite, and meteorological observations, *J. Geophys. Res.*, *116*, G00J07, doi:10.1029/2010JG001566.

Li, C., H. L. He, M. Liu, W. Su, Y. L. Fu, L. M. Zhang, X. F. Wen, and G. R. Yu (2008), The design and application of CO_2 flux data processing system at ChinaFLUX, *Geo Inf. Sci.*, *10*(5), 557–565.

Liburne, L., and S. Tarantola (2009), Sensitivity analysis of spatial models, *Int. J. Geogr. Inf. Sci.*, *23*(2), 151–168.

Lilburne, L., and S. Tarantola (2009), Sensitivity analysis of spatial models, *Int. J. Geogr. Inf. Sci.*, *23*(2), 151–168.

Lin, J. C., M. R. Pejam, E. Chan, S. C. Wofsy, E. W. Gottlieb, H. A. Margolis, and J. H. McCaughey (2011), Attributing uncertainties in simulated biospheric carbon fluxes to different error sources, *Global Biogeochem. Cycles*, *25*, GB2018, doi:10.1029/2010GB003884.

Lloyd, J., and J. A. Taylor (1994), On the temperature-dependence of soil respiration, *Funct. Ecol.*, *8*(3), 315–323.

Luis, S. J., and D. McLaughlin (1992), A stochastic approach to model validation, *Adv. Water Resour.*, *15*(1), 15–32.

McCallum, I., O. Franklin, E. Moltchanova, L. Merbold, C. Schmullius, A. Shvidenko, D. Schepaschenko, and S. Fritz (2013), Improved light and temperature responses for light-use-efficiency-based GPP models, *Biogeosciences*, *10*, 6577–6590.

Ogle, S. M., F. J. Breidt, M. Easter, S. Williams, K. Killian, and K. Paustian (2010), Scale and uncertainty in modeled soil organic carbon stock changes for US croplands using a process-based model, *Global Change Biol.*, *16*(2), 810–822.

Osmond, B., et al. (2004), Changing the way we think about global change research: Scaling up in experimental ecosystem science, *Global Change Biol.*, *10*(4), 393–407.

Papale, D., and A. Valentini (2003), A new assessment of European forests carbon exchanges by eddy fluxes and artificial neural network spatialization, *Global Change Biol.*, *9*(4), 525–535.

Papale, D., et al. (2006), Towards a standardized processing of Net Ecosystem Exchange measured with eddy covariance technique: Algorithms and uncertainty estimation, *Biogeosciences*, *3*(4), 571–583.

Potter, C. S., J. T. Randerson, C. B. Field, P. A. Matson, P. M. Vitousek, H. A. Mooney, and S. A. Klooster (1993), Terrestrial ecosystem production—A process model based on global satellite and surface data, *Global Biogeochem. Cycles*, *7*(4), 811–841.

Reich, P. B. (2010), The Carbon Dioxide Exchange, *Science*, *329*(5993), 774–775.

Reichstein, M., et al. (2005), On the separation of net ecosystem exchange into assimilation and ecosystem respiration: Review and improved algorithm, *Global Change Biol.*, *11*(9), 1424–1439.

Ren, X. L., H. L. He, L. Zhang, L. Zhou, G. R. Yu, and J. W. Fan (2013), Spatiotemporal variability analysis of diffuse radiation in China during 1981–2010, *Ann. Geophys.*, *31*(2), 277–289.

Running, S. W., P. E. Thornton, R. Nemani, and J. M. Glassy (2000), Global terrestrial gross and net primary productivity from the Earth Observing System, in *Methods in Ecosystem Science*, edited by O. E. Sala et al., pp. 44–57, Springer-Verlag, New York.

Saltelli, A. (2002), Making best use of model evaluations to compute sensitivity indices, *Comput. Phys. Commun.*, *145*(2), 280–297.

Shirmohammadi, A., et al. (2006), Uncertainty in TMDL models, *Trans. ASABE*, *49*(4), 1033–10.

Sobol, I. M. (1993), Sensitivity estimates for nonlinear mathematical models, *Math. Model. Comput. Experiment*, *1*(4), 407–414.

Tang, Y., P. Reed, K. van Werkhoven, and T. Wagener (2007), Advancing the identification and evaluation of distributed rainfall-runoff models using global sensitivity analysis, *Water Resour. Res.*, *43*, W06415, doi:10.1029/2006WR005813.

Tarantola, S., M. Nardo, M. Saisana, and D. Gatelli (2006), A new estimator for sensitivity analysis of model output: An application to the e-business readiness composite indicator, *Reliab. Eng. Syst. Safe.*, *91*(10–11), 1135–1141.

Taylor, K. E. (2001), Summarizing multiple aspects of model performance in a single diagram, *J. Geophys. Res.*, *106*(D7), 7183–7192.

The Compiling Committee of the Atlas of Grassland Resources of China (1993), *The Atlas of Grassland Resources of China*, SinoMaps Press, Beijing.

Vermote, E. F., and S. Kotchenova (2008), Atmospheric correction for the monitoring of land surfaces, *J. Geophys. Res.*, *113*, D23S90, doi:10.1029/2007JD009662.

Verstraeten, W. W., F. Veroustraete, W. Heyns, T. Van Roey, and J. Feyen (2008), On uncertainties in carbon flux modelling and remotely sensed data assimilation: The Brasschaat pixel case, *Adv. Space Res.*, *41*(1), 20–35.

Wang, H. S., G. S. Jia, C. B. Fu, J. M. Feng, T. B. Zhao, and Z. G. Ma (2010), Deriving maximal LUE from coordinated flux measurements and satellite data for regional gross primary production modeling, *Remote Sens. Environ.*, *114*(10), 2248–2258.

Webb, E. K., G. I. Pearman, and R. Leuning (1980), Correction of flux measurements for density effects due to heat and water vapor transfer, *Q. J. R. Meteorol. Soc.*, *106*(447), 85–100.

Wu, C. Y., Z. Niu, and S. A. Gao (2010), Gross primary production estimation from MODIS data with vegetation index and photosynthetically active radiation in maize, *J. Geophys. Res.*, *115*, D12127, doi:10.1029/2009JD013023.

Wylie, B. K., E. A. Fosnight, T. G. Gilmanov, A. B. Frank, J. A. Morgan, M. R. Haferkamp, and T. P. Meyers (2007), Adaptive data-driven models for estimating carbon fluxes in the Northern Great Plains, *Remote Sens. Environ.*, *106*(4), 399–413.

Xiao, J. F., K. J. Davis, N. M. Urban, K. Keller, and N. Z. Saliendra (2011), Upscaling carbon fluxes from towers to the regional scale: Influence of parameter variability and land cover representation on regional flux estimates, *J. Geophys. Res.*, *116*, G00J06, doi:10.1029/2010JG001568.

Xiao, J., et al. (2008), Estimation of net ecosystem carbon exchange for the conterminous United States by combining MODIS and AmeriFlux data, *Agric. For. Meteorol.*, *148*(11), 1827–1847.

Xiao, X. M., D. Hollinger, J. Aber, M. Goltz, E. A. Davidson, Q. Y. Zhang, and B. Moore (2004a), Satellite-based modeling of gross primary production in an evergreen needleleaf forest, *Remote Sens. Environ.*, *89*(4), 519–534.

Xiao, X. M., Q. Y. Zhang, B. Braswell, S. Urbanski, S. Boles, S. Wofsy, M. Berrien, and D. Ojima (2004b), Modeling gross primary production of temperate deciduous broadleaf forest using satellite images and climate data, *Remote Sens. Environ.*, *91*(2), 256–270.

Yan, H., Y. Fu, X. Xiao, H. Q. Huang, H. He, and E. Laura (2009), Modeling gross primary productivity for winter wheat-maize double cropping system using MODIS time series and CO_2 eddy flux tower data, Agric, *Ecosyst. Environ.*, *129*, 391–400.

Yang, F., et al. (2007), Developing a continental scale measure of gross primary production by combining MODIS and AmeriFlux data through support vector machine approach, *Remote Sens. Environ.*, *110*, 109–122.

Yang, Y. H., J. Y. Fang, P. A. Fay, J. E. Bell, and C. J. Ji (2010), Rain use efficiency across a precipitation gradient on the Tibetan Plateau, *Geophys. Res. Lett.*, *37*, L15702, doi:10.1029/2010GL043920.

Yu, G. R., X. F. Wen, X. M. Sun, B. D. Tanner, X. H. Lee, and J. Y. Chen (2006), Overview of ChinaFLUX and evaluation of its eddy covariance measurement, *Agric. For. Meteorol.*, *137*(3–4), 125–137.

Yuan, W., et al. (2007), Deriving a light use efficiency model from eddy covariance flux data for predicting daily gross primary production across biomes, *Agric. For. Meteorol.*, *143*(3–4), 189–207.

Zhang, Y. Q., Q. Yu, J. Jiang, and Y. H. Tang (2008), Calibration of Terra/MODIS gross primary production over an irrigated cropland on the North China Plain and an alpine meadow on the Tibetan Plateau, *Global Change Biol.*, *14*(4), 757–767.

Zhang, L., B. K. Wylie, L. Ji, T. G. Gilmanov, L. L. Tieszen, and D. M. Howard (2011), Upscaling carbon fluxes over the Great Plains grasslands: Sinks and sources, *J. Geophys. Res.*, *116*, G00J03, doi:10.1029/2010JG001504.

Zhu, X. D., H. L. He, M. Liu, G. R. Yu, X. M. Sun, and Y. H. Gao (2010), Spatio-temporal variation of photosynthetically active radiation in China in recent 50 years, *J. Geogr. Sci.*, *20*(6), 803–817.

Zhuang, Q., et al. (2003), Carbon cycling in extratropical terrestrial ecosystems of the Northern Hemisphere during the 20th century: A modeling analysis of the influences of soil thermal dynamics, *Tellus*, *55B*, 751–776.

Zhuang, Q., J. He, Y. Lu, L. Ji, J. Xiao, and T. Luo (2010), Carbon dynamics of terrestrial ecosystems on the Tibetan Plateau during the 20th century: An analysis with a process-based biogeochemical model, *Global Ecol. Biogeogr.*, *19*(5), 649–662.